Title	Structure analysis of a buried interface between organic and porous inorganic layers using spin-contrast-variation neutron reflectivity
Author(s)	Kumada Takayuki, Miura Daisuke, Akutsu Kazuhiro, Oishi Kazuki, Morikawa Toshiaki, Kawamura Yukihiko, Suzuki Junichi, Oku Takayuki, Torikai Naoya, Niizeki Tomotake
Citation	Journal of Applied Crystallography, 55(5), p.1147-1153
Text Version	Accepted Manuscript
URL	https://jopss.jaea.go.jp/search/servlet/search?5074212
DOI	https://doi.org/10.1107/S1600576722007506
Right	© International Union of Crystallography

Structure analysis of a buried interface between organic and porous inorganic layers using spin-contrast-variation neutron reflectivity

Authors

Takayuki Kumada[a]*, Daisuke Miura[b], Kazuhiro Akutsu−Suyama[c], Kazuki Ohishi[c], Toshiaki Morikawa[c], Yukihiko Kawamura[c], Jun-ichi Suzuki[c], Takayuki Oku[d], Naoya Torikai[e] and Tomotake Niizeki[f]

[a]Materials Sciences Research Center, Japan Atomic Energy Agency, Tokai, Ibaraki, 319-1195, Japan
[b]Department of Physics, Yamagata University, Yamagata 990-8560, Japan
[c] Neutron Science and Technology Center, Comprehensive Research Organization for Science and Society (CROSS), Tokai, Ibaraki 319-1106, Japan
[d]J-PARC Center, Japan Atomic Energy Agency, Tokai, Ibaraki 319-1195, Japan
[e]Graduate School of Engineering, Mie University, Tsu, Mie 514-8507, Japan
[f]ART KAGAKU Co., Ltd., Muramatsu, Tokai, Ibaraki 319-1112, Japan.

Correspondence email: kumada.takayuki@jaea.go.jp

Synopsis Spin-contrast-variation neutron reflectivity obtains multiple reflectivity curves from a single sample and a single beam source. We used the strong point of the technique to reveal that, although methylated-perhydropolysilazane-derived silica layer has a higher porosity near the interface with acrylic urethane resin, the resin did not permeate the pore network.

Abstract We demonstrate the advantage of spin-contrast-variation neutron reflectivity (NR) for the structure analysis of a buried interface in a bilayer film between the organic and inorganic layers of acrylic urethane resin and methylated silica (MePDS), which was derived from methyl-group-substituted perhydropolysilazane. As proton polarization P_H changed from 0% to ±24%, the NR curve of the bilayer film varied remarkably. These NR curves were not reproduced using global fitting with a standard bilayer model. The oscillation in the NR curve at P_H = -24% was shifted slightly and non-negligibly from the fitting curve using the best-fit structure parameters for the curve at P_H = 0%. We found from the shift of the oscillation that the density of the MePDS layer decreased within several nanometers of the interface, but the resin did not permeate the MePDS layer.

Keywords: Spin-contrast-variation neutron reflectivity; Buried interface; Organic-inorganic hybrid material.

1. Introduction

Nano-ordered organic-inorganic composite materials, known as hybrid materials, which consist of a molecular-level dispersion of organic and inorganic components, have been attracting attention for their

use in high-functionality materials. The high degree of control over the composition and nanostructure of the materials results in improved mechanical, thermal, electrical, optical, and chemical properties compared with the organic or inorganic materials alone (Srivastava, 2013).

The nanostructure analysis of the interface between the organic and inorganic components is important in the development of the hybrid materials because strong coupling between these components is essential for achieving the functionality. For example, small voids between the polymer and SiO_2 or SiC nanocomposites for power electronics devices reduce discharge endurance (Tanaka *et al.*, 2004; Tanaka, 2005). Chemical bridging between rubber and silica in car tires is essential to increase elasticity and decrease inner friction (Sengloyluan *et al.*, 2014). Systematic investigation of structure–property relationships will greatly advance the development of hybrid materials.

Neutron reflectivity (NR) and X-ray reflectivity (XR) are promising techniques that non-destructively measure the structure of buried interfaces between organic and inorganic layers in a multilayer film. NR has an advantage over XR for measuring buried interfaces because of the higher transmission of neutron beams (Russsell, 1990; Stoev & Sakurai, 2020). Since the number of structure parameters of multilayer films is too large to determine the structure of the buried interface using a single NR curve, several contrast variation techniques, such as deuterium contrast variation (Crowly *et al.*, 1991; Heinrich, 2016), magnetic contrast variation (Majkrzak *et al.*, 1999), combined NR and XR (Nelson, 2006), and resonant XR (Wang, 2007), have been developed. However, these techniques have various limitations.

To overcome these limitations, we recently applied spin-contrast-variation (SCV), which has been used for small-angle neutron scattering (SANS), to NR (Kumada *et al.,* 2019). SCV relies on the large variation of the coherent polarized neutron scattering length of a proton, b_H, as a function of the proton polarization, P_H, against the neutron spin direction (Knop *et al*., 1989; Knop *et al*., 1991),

$$b_H(P_H) = [-0.374 + 1.456\ P_H] \times 10^{-12}\ \text{(cm)}. \quad (1)$$

Thus, as P_H increases, the scattering length density (SLD), which is the sum of the scattering length of atoms in a unit volume, of each layer of a multilayer film increases proportionally with the proton number density (Knop *et al*., 1991; Sears, 1992; Brandrup *et al*., 1999). The variation of SLD results in the variation of the NR curve. Multiple structure parameters of the multilayer films are determined by the P_H-dependent multiple NR curves.

We have developed methylated silica (MePDS) derived from methyl-group-substituted perhydropolysilazane (Me-PHPS) as a primer coating material for use between inorganic and organic materials (Niizeki *et al.*, 2016; Akutsu *et al.*, 2018). To prevent peeling and cracking due to thermal expansion and contraction of organic components, MePDS was made more flexible than conventional perhydropolysilazane (PHPS)-derived silica (PDS) by the partial substitution of oxygen, which bridges neighbouring Si atoms via a Si-O-Si bond, with a methyl group. In addition, because the methyl group

is hydrophobic, it is expected that MePDS binds to organic resins more strongly than PDS.

SCV is good for the structure analysis of composite materials that are composed of high-and low-hydrogen-content layers, such as organic and inorganic materials. Generally, the SLD of organic materials varies with P_H much more than that of inorganic materials because the number density of hydrogen in organic materials is much higher than that of inorganic materials. Thus, the scattering intensity, which is proportional to the square of the difference in their SLDs, varies greatly as a function of P_H. We previously used SCV for SANS measurements of the assembled structure of silica nanoparticles in model systems for car tires (Noda *et al.*, 2016). In this study, we applied SCV-NR to the structure analysis of the buried interface between acrylic urethane resin and MePDS. We demonstrated that SCV-NR is also useful for the structure analysis of organic-inorganic hybrid materials.

2. Experiment

2.1. Sample

The sample was a bilayer film of acrylic urethane resin on MePDS. The MePDS layer was prepared by spin-coating a mixture of 3% PHPS (AZ Electronic Materials Co., Ltd., Tokyo, Japan) and 1% Me-PHPS (Akutsu *et al.*, 2018) in xylene. After a 25 × 25 × 1 mm single-crystal Si substrate was covered with the solution, it was rotated at a speed of 6000 rpm for 60 s using a spin-coater (MS-A150, Mikasa Co., Ltd., Tokyo, Japan), and allowed to stand for 1 week at room temperature. The acrylic urethane resin was composed of acrylic polyol and polyisocyanate (Utanal (L) Clear, Ohashi Chemical Industries Ltd., Osaka, Japan). The thinner (No. 7400), composed of toluene, methanol, and ethyl acetate, was doped with 3.3 mM 4-methacryloyloxy-2,2,6,6-tetramethylpiperidine 1-oxyl free radical (TEMPO methacrylate, Aldrich, 730297) as a polarizing agent beforehand. Within a few minutes of the main resin, curing agent (M-60), and thinner being mixed at a volume ratio of 4:1:45, the solution was spin-coated on the MePDS-coated Si substrate at a speed of 6000 rpm for 60 s. The film was then cured at 60 °C for 12 h. The thinner evaporated, and thus the concentration of the polarizing agent in the resin increased to 34 mM. Elemental analysis of the MePDS powder was conducted at the Center of Instrumental Analysis, Ibaraki University. Anal. calcd. for $CH_{3.25}O_{2.75}N_{0.25}Si$: C, 10.10; H, 2.76; N, 2.94. Found: C, 9.99; H, 3.33; N, 2.69.

2.2. Proton polarization

The protons in the film samples were polarized using dynamic nuclear polarization (DNP), in which the nuclear spins are hyperpolarized by polarization transfer from electron spins in the polarizing agent to the nuclear spins (Wenckebach, 2016). In this study, instead of the cryogen-free apparatus used in the previous SCV-NR measurements (Kumada *et al.*, 2018, 2019), we used conventional cryogen-filled DNP apparatus (Kumada *et al*., 2009) for the SCV-NR measurements because we expected higher P_H

can be obtained due to the higher cooling power. The DNP apparatus comprised a horizontal-field superconducting Helmholtz coil magnet (JMTC-3.5T/50/SP, JASTEC, Tokyo, Japan) with a cryostat, microwave devices, and a proton nuclear magnetic resonance (NMR) circuit. The sample in the cryostat was cooled to 1.2 K by pumping liquid helium with a serially connected dry pump (NeoDry60E, Kashiyama, Tokyo, Japan) and two booster pumps (SMB-C06 and SMB-C25, Shinko Seiki, Kobe, Japan). The sample was irradiated with microwaves with a frequency of 94 GHz from a Gunn oscillator (VCO-10-9415-10RI, VCSS, Rancho Palos Verdes, CA) and the amplifier (AMP-10-01300, Millitech, Northampton, MA) at 3.3 T to transfer polarization from electrons in the free radicals to protons. Because the number of protons in the film sample was too small to observe an NMR signal, we monitored the dynamically polarized proton signals of a 33 mM 2,2,6,6-tetramethylpiperidine 1-oxyl (TEMPO)-doped polystyrene reference sample, which was set 17 mm above the film sample to tune the magnetic field and microwave frequency and power.

2.3. NR measurement

The SCV-NR measurements were performed by placing the DNP apparatus in the SHARAKU polarized neutron reflectometer (BL17) of the Materials and Life Science Experimental Facility (MLF) at the Japan Proton Accelerator Research Complex (J-PARC) (Takeda *et al*., 2012; Akutsu-Suyama *et al*., 2020). Pulsed neutrons with a wavelength (λ) range of 0.24–0.88 nm were polarized up to 98.5% using a polarizing Fe/Si supermirror, and then irradiated at the incident angle $\theta = 0.3°$, 0.9°, and 2.7° from the free-surface side of the film samples on the Si substrates. The spot size of the neutron beam was 20 mm high and 15 mm wide and was maintained by adjusting the slit width every time θ was changed. The unpolarized neutron reflectivity (UNR) curve was measured using unpolarized neutron beams and the unpolarized sample, whereas the polarized NR curves were measured using polarized neutrons and the proton-polarized sample. The polarization of the incident neutrons was inverted in parallel and perpendicular to the proton polarization every 30 s to measure the positively polarized neutron reflectivity (PNR) and negatively polarized reflectivity (NNR) curves almost simultaneously. All the NR measurements were carried out at 1.2 K in liquid helium. The NR curves were analyzed using the Motofit program (Nelson, 2006).

3. Results and analysis

3.1. Results

The symbols in Fig. 1 show the UNR, PNR, and NNR curves of the film sample as a function of the magnitude of the scattering vector Q,

$$Q = 4\pi\sin\theta/\lambda. \quad (2)$$

The oscillations with periods of 0.1 and 0.03 nm^{-1} are related to the thicknesses of the MePDS and resin layers, respectively. The reflectivity of the PNR and NNR curves are much higher than that of the UNR curve over the whole Q range. The critical Q value of the total reflection of the PNR curve is much higher than that of the UNR and NNR curves, indicating that total reflection occurs at the resin layer in the PNR curve, but at the Si substrate in the UNR and NNR curves (see 3.2. for detail). The visibility of the oscillation, which corresponds to the oscillation amplitude in the logarithmic graph, of the NNR curve is higher than that of the UNR curve, but that of the PNR curve is lower. This result suggests that, as P_H increases, the reflection amplitudes at specific surfaces or interfaces become higher than those at the others. The intensity of the background electronic noise signal, which is observed as a plateau at the high-Q limit, of the PNR and NNR curves is twice as large as that of the UNR curve. Because the intensity of the incident polarized neutron beam is approximately half of that of the unpolarized beam, the intensity of the background signal that is normalized by the incident beam intensity of the PNR and NNR curves becomes larger than that of the UNR curve.

3.2. Analysis using the standard model

The solid lines in Fig. 1 show the global fitting curves using a standard bilayer model. The inset shows the SLD profiles used for the fitting of the UNR, PNR, and NNR curves with a common set of structure parameters and P_H-dependent SLDs for the resin, ρ_r^0, ρ_r^+, ρ_r^-, and for MePDS, ρ_s^0, ρ_s^+, ρ_s^-, that are restricted to the calculated SLD $\rho_i(P_H)$,

$$\rho_r^0 = \rho_r(0), \tag{3}$$

$$\rho_r^+ = \rho_r(+P_{DNP}), \tag{4}$$

$$\rho_r^- = \rho_r(-P_{DNP}), \tag{5}$$

$$\rho_s^0 = \rho_s(0), \tag{6}$$

$$\rho_s^+ = \rho_s(+P_{DNP}), \tag{7}$$

$$\rho_s^- = \rho_s(-P_{DNP}). \tag{8}$$

where P_{DNP} is absolute value of proton polarization of the polarized sample. It should be stressed that P_H in the MePDS layer is the same as that in the resin layer because P_H in organic materials is homogenized up to the micrometer length scale due to the spin-diffusion in our DNP conditions (Miura *et al.*, 2021). $\rho_i(P_H)$ is obtained by substituting density d_i, elemental composition N_j^i, coherent polarized-neutron scattering length b_j, and mass m_j of element j in resin (i = r) and MePDS (i = s) into

$$\rho_i(P_H) = d_i \frac{N_H^i b_H(P_H) + \sum_{j \neq H} N_j^i b_j}{\sum_j N_j^i m_j}, \quad i = \{r, s\}. \tag{9}$$

The polarization dependences of the scattering length of nuclei other than H are so small that they are neglected. It is convenient to determine ρ_r^+ by substituting the critical Q value of the total reflection of the PNR curve Q_c^+ and SLD of liquid He ρ_{He} into the equation (Imae *et al.*, 2011),

$$Q_c^+ = 4\sqrt{\pi(\rho_r^+ - \rho_{He})}, \quad (10)$$

and then finding the other SLDs and structure parameters.

Fig. 2 shows the best-fit SLDs, $\rho_r(P_H)$ and $\rho_s(P_H)$, which are obtained using d_r = 1.30 g/cm^3, d_s = 1.30 g/cm^3. P_{DNP} = 24% was also determined by substituting ρ_r^+ into Eq. (4). d_r is close to densities of the main components of the resin, poly(methyl methacrylate) (1.2 g/cm^3) and poly(urethanes) (1.1−1.5 g/cm^3) (Brandrup *et al.*, 1999), whereas d_s is much smaller than the density of silica (2.65 g/cm^3) because a nano and micropore network is generated in polymer-derived ceramics (Wilhelm *et al.,* 2005; Konegger *et al.*, 2016, 2021; Akutsu *et al.*, 2018). The porosity of spin-coated PDS is estimated to be 40% from the ratio in SLD between PDS and bulk silica (Akutsu *et al*., 2018), and thus that of MePDS is expected to be comparable.

The fitting curves reproduce the UNR and PNR curves, but not the NNR curve. The phase of the oscillation with a period of 0.1 nm^{-1} in the NNR curve is shifted from that in the simulation using the best-fit structure parameters for the UNR curve. The oscillation is caused by the interference of reflected neutrons from the resin-MePDS interface and Si substrate. The distance between them is determined as 64 nm from the analysis of the UNR curve but as 66 nm from the NNR curve.

3.3. Analysis using the permeation model

Because the standard model uses a Gaussian smearing function to characterize the roughness and diffuseness of surfaces and interfaces, it cannot represent asymmetric roughness and diffuseness across an interface (Mizusawa & Sakurai, 2003). The fitting assumes that, from the MePDS layer to the resin layer across the interface, the pore network and MePDS are substituted for the resin at the same ratio (Fig. 3 (a)). If the resin permeates the pore of the MePDS layer, the porosity in the permeated volume will be lower than that in the MePDS layer (Fig. 3 (b)). We searched for the best-fit parameter using the permeation model, which has the resin-permeated low-porosity MePDS sublayer (permeated sublayer) between the resin and MePDS layers. However, the deviation in the oscillation phase between the NNR curve and its fitting is worse than that in the standard model (not shown). This result indicates that the resin does not permeate into the pore network of the MePDS layer.

3.4. Analysis using the density gradient model

The density of a spin-coated PDS film within a few nanometers of the surface is lower than that inside

the film (Akutsu-Suyama *et al.*, 2020). Thus, a similar density gradient is expected to occur near the interface of the MePDS layer of the film sample. The solid lines in Fig. 4 show the global fitting of the UNR, PNR, and NNR curves with the model in which the resin does not permeate the MePDS layer, and the density of the MePDS layer gradually decreases by 35% within 2.5 nm of the interface (Fig. 3 (c)). In other words, the porosity in the density gradient is higher than that inside the MePDS layer.

The inset in Fig. 4 shows the SLD profiles used for the fitting. The fitting curves reproduce all the UNR, PNR, and NNR curves, including the phase of the oscillation, much better than those in Fig. 1. Because the increase in SLD at the resin-MePDS interface (Blue arrow in the inset) is much larger than that at the density gradient in the negatively polarized sample, the reflection amplitude at the interface is much larger. Thus, oscillation periods in the NNR curves are determined by the distances from the free surface and Si substrate to the interface. In contrast, because the increase in SLD at the density gradient (Black arrow in the inset) is larger than that at the interface in the unpolarized sample, the reflection amplitude at the density gradient is larger. Thus, the oscillation period in the UNR curve is determined by the distances to the density gradient rather than to the interface. The thickness of the density gradient from the interface is determined to be 2.5 nm from the difference in the oscillation period between the NNR and UNR curves.

4. Discussion

This fitting result reveals that although the porosity near the interface of the MePDS layer is higher than that inside, the resin does not permeate the pore network. Because the resin and curing agent were mixed before the spin-coating, they were polymerized before permeation, the polymer was probably too large to permeate the pore network of the MePDS layer. This is not desirable for manufacturing hybrid materials because a smaller contact area between the resin and MePDS results in a higher risk of detachment. To decrease the risk, we propose that the pore network near the interface is permeated with the resin and curing agent successively before spin-coating of the resin layer. If only the resin and curing agent permeate successively, they will polymerize in the pore network (Fig. 3 (b)), and the polymer chains that extend from the pore will be entangled with those in the resin layer.

The advantage of the SCV-NR technique is that multiple NR curves can be obtained from a single sample with a single beam source. We used SCV-NR to discriminate between the reflected neutrons from the interface itself and the density gradient near the interface. However, other contrast variation techniques would struggle to discriminate between these two reflections. For example, even if we observe such a small difference in oscillation period between multiple NR curves from multiple partially deuterated samples in deuterium contrast variation measurements, we would suspect that the difference could arise from the structural reproducibility between samples. It would be more difficult to compare XR and NR curves than to compare SCV-NR curves because the coherent length of beams and optical layouts, which determine properties including resolution and experimental error, of the XR and NR

measurements, are different for these curves. Magnetic contrast variation cannot vary contrast between non-magnetic layers. Resonant soft X-ray reflectivity (RSoXR) may be able to discriminate, because both RSoXR and SCV-NR change the contrast using a single sample and a single beam source. SCV-NR controls b_H with polarizing protons, whereas RSoXR controls the scattering lengths of carbon and heavier elements by tuning soft X-ray energy close to the absorption edges of light atoms (Wang *et al.*, 2007). We should recognize the advantages of SCV-NR and other contrast variation techniques, such as RSoXR, for the structure analyses of buried interfaces.

Currently, doping of nonvolatile polarizing agents is the most difficult point of SCV-NR measurements. We use TEMPO methacrylate rather than TEMPO, which is generally used for polarization of bulk samples, because TEMPO methacrylate does not vaporize from the surface of the nanometer-thick film samples at room temperature. However, it vaporizes when the sample is annealed at higher temperatures. To overcome the problem, we are developing a technique to dope vaporized TEMPO methacrylate and/or other TEMPO derivatives into polymer samples at higher temperatures. The vapor-doping technique was established for TEMPO (Bunyatova, 1995), but not for TEMPO methacrylate and other derivatives due to lower volatility and lager molecular size. Such improvements of the doping technique will extend the applicability of the SCV-NR technique to a wider variety of samples.

5. Conclusion

We used SCV-NR for the structure analysis of the interface between acrylic urethane resin and MePDS layers in a thin film. The UNR, PNR, and NNR curves of the film were not reproduced by the global fitting with a standard bilayer model. In particular, the phase of the oscillation with a period of approximately 0.1 nm^{-1} in the NNR curve was slightly but non-negligibly shifted from that of the simulation curve using the best-fit structure parameters for the UNR curve. The model assuming the permeation of the resin into the pore network of the MePDS layer resulted in worse fitting, that is, a larger shift in the oscillation phase. In contrast, the three NR curves were globally fitted with the model in which the MePDS layer density gradually decreased by 35% within 2.5 nm of the interface and the porosity increased complimentarily. This fitting result revealed that although a larger pore volume was generated near the MePDS layer interface, the resin did not permeate the pore network. Such structural information at the interface is important on the development of hybrid material. We will establish the SCV-NR technique as a tool in quality managements.

Acknowledgments

We are grateful to Dr. R. Motokawa of JAEA for fruitful comments and suggestions on the analysis. Samples were prepared at the User Experiment Preparation Lab III that is provided by CROSS. Neutron reflectivity measurements were conducted as part of proposal Nos. 2018P0203, 2019P0203, and 2020P0203 at the J-PARC MLF.

Funding Information

This work was supported in part by the JAEA fund for Exploratory Researches (Houga fund) and Grant-in-Aid for Scientific Research from the Ministry of Education, Culture, Sports, Science and Technology, Japan (No. 18K11926, 21H03741).

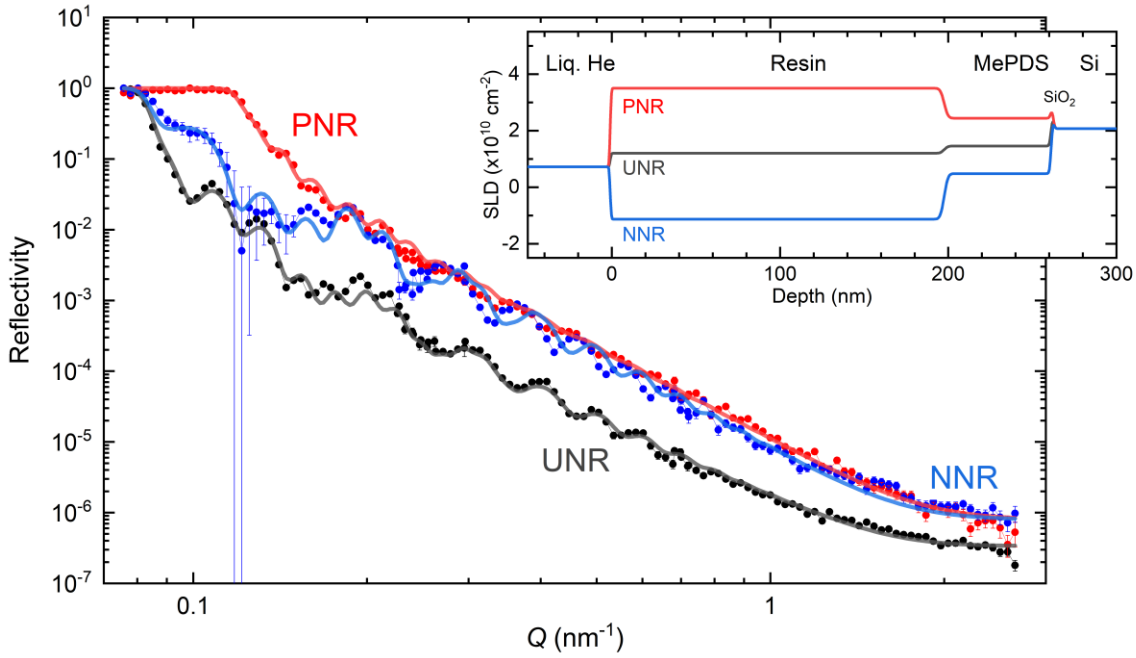

Figure 1 SCV-NR curves of the resin-on-MePDS bilayer film. Solid lines show the best-fit simulation curves using the standard bilayer model with SLD profiles in the inset. The structure parameters used for the fitting are shown in Table S1.

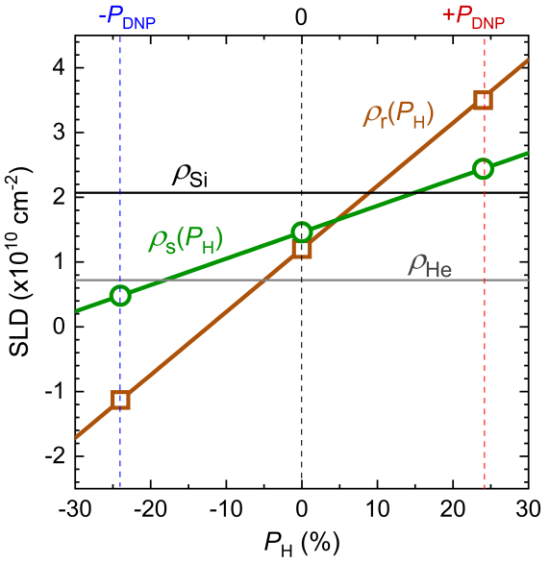

Figure 2 $\rho_r(P_H)$ and $\rho_s(P_H)$ calculated using $d_r = 1.30$ g/cm^3 and $d_s = 1.30$ g/cm^3. Squares at $P_H = 24\%$, 0%, and -24% are ρ_r^+, ρ_r^0, and ρ_r^-, respectively, and circles are ρ_s^+, ρ_s^0, and ρ_s^-.

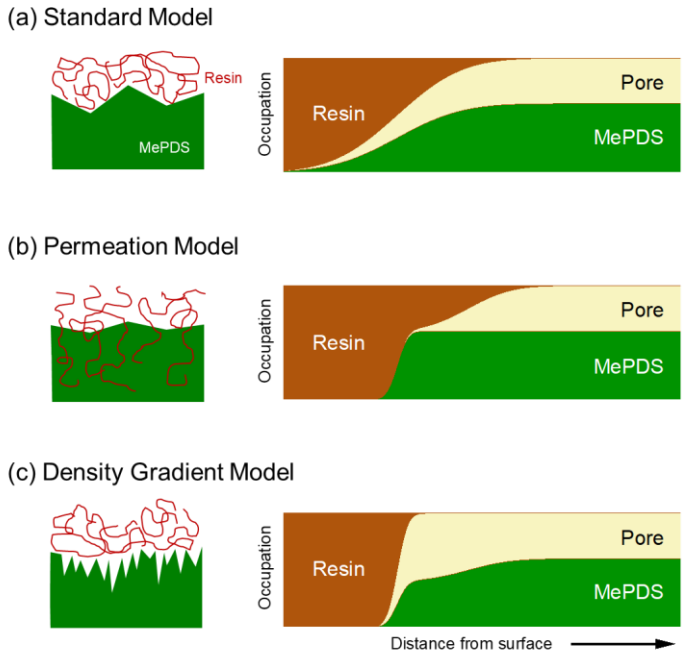

Figure 3 Schematic images and in-depth occupation profiles of the resin-MePDS interface.

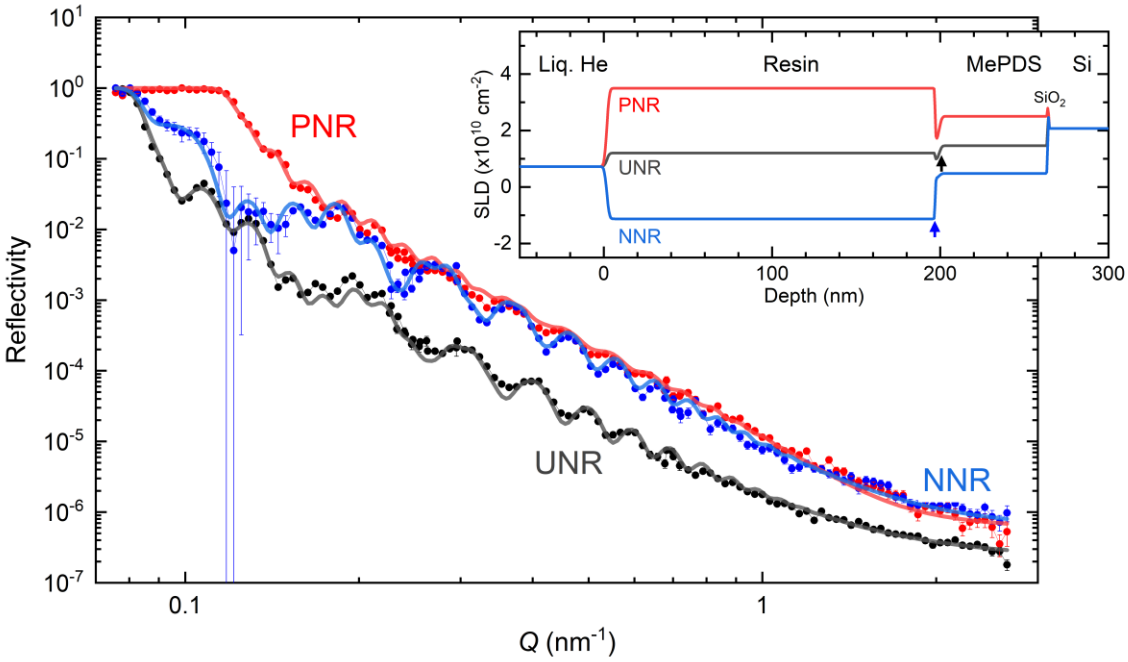

Figure 4 Same experimental data as in Fig. 1, but simulated using the density gradient model with SLD profiles in the inset. The structure parameters used for the fitting are shown in Table S2.

Acknowledgements We are grateful to Dr. R. Motokawa of JAEA for fruitful discussions and suggestions about the analysis. Samples were prepared at the User Experiment Preparation Lab III that is provided by the Comprehensive Research Organization for Science and Society (CROSS). Neutron reflectivity measurements were conducted as part of proposal Nos. 2018P0203, 2019P0203, and 2020P0203 at the J-PARC MLF.

References

Akutsu, K., Sahara, M., Niizeki, T., Nagayama, S., Hasegata, Y., Shimomura, A., Komatsuzaki, H. (2018). *Proceedings of the 15th annual meeting of particle accelerator society of Japan,* 1198–1201.

Akutsu-Suyama, K., Kira, H., Miyata, N., Hanashima, T., Miyazaki, T., Kasai, S., Yamazaki, D., Soyama, K., & Aoki, H., (2020). *Polymers* **12**, 2180.

Brandrup, J., Immergut, E. H. & Grulke, E. A. (1999). *Polymer handbook, 4th ed.* New York: Wiley-interscience.

Bunyatova, E. I. (1995). *Nucl. Inst. Meth. A* **356**, 29-33.

Crowley, T. L., Lee, E. M., Simister, E. A. & Thomas, R. K. (1991). *Physica B* **173**, 143–156.

Heinrich, F. (2016). *Methods Enzymol.* **566**, 211–230.

Imae, T., Kanaya, T., Furusaka, M. & Torikai, N. (2011). *Neutrons in soft matter,* p. 115–145. Hoboken: Wiley & Sons.

Knop, W., Hirai, M., Olah, G., Meerwinck, W., Schink, H.-J., Stuhrman, H. B., Wagner, R., Wenkow-EsSouni, M., Zhao, J., Schärpf, O., Crichton, R. R., Krumpolc, M., Nierhaus, K. H., Niinikoski, T. O. & Rijllart, A. (1991). *Physica B* **174**, 275–290.

Knop, W., Schink, H.-J., Stuhrmann, H. B., Wagner, R., Wenkow-Es-Souni, M., Schärpf, O., Krumpolc, M., Niinikoski, T. O., Rieubland, M. & Rijllart, A. (1989). *J. Appl. Cryst.* **22**, 352–362.

Konegger, T., Tsai, C., Peterlik, H., Creager, S. E. & Bordia, R. K. (2016). *Microporous Mesoporous Mater.* **232**, 196-204.

Konegger, T., Drechsel, C. & Peterlik, H. (2021). *Microporous Mesoporous Mater.* **324**, 111268.

Kumada, T., Akutsu, K., Ohishi, K., Morikawa, T., Kawamura, Y., Sahara, M., Suzuki, J. & Torikai, N. (2019). *J. Appl. Cryst.* **52**, 1054–1060.

Kumada, T., Akutsu, K., Ohishi, K., Morikawa, T., Kawamura, Y., Sahara, M., Suzuki, J. & Torikai, N. (2018). *JPS Conf. Proc.* **22**, 011015.

Kumada, T., Noda, Y., Hashimoto, T. & Koizumi, S. (2009). *Nucl. Inst. Meth. A* **606**, 669–674.

Majkrzak, C. F. & Berk, N. F. (1999). *Physica B* **267**–**268**, 168–174.

Miura, D., Kumada, T., Sekine, Y., Motokawa, R., Nakagawa, H., Oba, Y., Ohhara, T., Takata, S., Hiroi, K., Morikawa, T., Kawamura, Y., Ohishi, K., Suzuki, J., Miyachi, Y., Iwata, T., (2021). *J. Appl. Cryst.* **54**, 454-460.

Mizusawa, M. & Sakurai, K. (2003). *Jpn. J. Appl. Phys.* **42**, 3709-3710.

Nelson, A. (2006). *J. Appl. Cryst*. **39**, 273–276.

Niizeki, T., Nagayama, S., Hasegawa, Y., Shimomura, A., Sahara, M., Miyata, N., & Akutsu, K. (2016). *Proceedings of the 13th annual meeting of particle accelerator society of Japan,* 1240–1243.

Noda, Y., Koizumi, S., Masui, T., Mashita, R., Kishimoto, H., Yamaguchi, D., Kumada, T., Takata, S., Ohishi, K. & Suzuki, J. (2016) *J. Appl. Cryst.* **49**, 2036–2045.

Russell, T. P. (1990). *Mater. Sci. Rep.* **5**, 171–271.

Sears, V. F. (1992). *Neutron News* **3**, 26–37.

Sengloyluan, K, Sahakaro, K, Dierkes, & W. K., Noordermeer, J. W. M. (2014). *Euro. Polym. J.* **51,** 69–79.

Srivastava, N. (2013). *Organic-Inorganic hybrid materials,* Lap Lambert.

Stoev, K. & Sakurai, K. (2020). *Anal. Sci.* **36**, 901–922.

Takeda, M., Yamazaki, D., Soyama, K., Maruyama, R., Hayashida, H., Asaoka, H., Yamazaki, T., Kubota, M., Aizawa, K., Arai, M., Inamura, Y., Ito, T., Kaneko, K., Nakamura, T., Nakatani, T., Oikawa, K., Ohara, T., Sakaguchi, Y., Sakasai, K., Shinohara, T., Suzuki, J., Suzuya, K., Tamura, I., To, K., Yamagishi, H., Yoshida, N. & Hirano, T. (2012). *Chi. J. Phys.* **50**, 161–170.

Tanaka, T. (2005). IEEE Trans. *Dielecr. Electr. Insul.* **12**, 914–928.

Tanaka, T., Montanari, G. & C., Mülhaupt, R. (2004). *IEEE Trans. Dilectr. Electr. Insul.* **11**, 763–784.

Wang, C., Araki, T., Watts, B., Harton, S.k Koga, T., Basu, S., Abe, H. (2007). *J. Vac. Sci. Technol. A* **25**, 575–586.

Wenckebach, T. (2016). *Essentials of Dynamic Nuclear Polarization.* Spindrift.

Wilhelm, M., Soltmann, C., Koch, D. & Grathwohl, G. (2005). *J. Eur. Ceram. Soc.* **25**, 271-276.

Supporting information

Table S1 Thickness, SLD, and surface and interface roughness for the MOTOFIT simulation in Fig. 1.

	Thickness (nm)	SLD ($\times 10^{10}$ cm^{-2})			Roughness (nm)
		UNR	PNR	NNR	
Liq. He			0.72		
Resin	198.0	1.20	3.50	-1.13	0.5
MePDS	63.7	1.46	2.50	0.48	1.8
SiO_2	0.641		3.47		0.85
Si			2.07		0.85

Table S2 Thickness, SLD, and surface and interface roughness for the MOTOFIT simulation in Fig. 4.

	Thickness (nm)	SLD ($\times 10^{10}$ cm^{-2})			Roughness (nm)
		UNR	PNR	NNR	
Liq. He			0.72		
Resin	198.0	1.20	3.50	-1.13	1.2
[*1]MePDS	2.5	0.95	1.63	0.34	0.3
MePDS	65.4	1.46	2.50	0.48	1.2
SiO_2	0.391		3.47		0.3
Si	-		2.07		0.3

[*1] Near the interface with the resin layer